Böttcher, René; Mai, Sebastian; Ispas, Adriana; Bund, Andreas:

Aluminum deposition and dissolution in [EMIm]Cl-based ionic liquids-kinetics of charge-transfer and the rate-determining step

Original published in:	Journal of the Electrochemical Society / Electrochemical Societyristol : IOP Publishing. - 167 (2020), 10, art. 102516, 8 pp.
Original published:	2020-06-29
ISSN:	1945-7111
DOI:	10.1149/1945-7111/ab9c84
[*Visited:*	2020-11-20]

Journal of The Electrochemical Society, 2020 **167** 102516

Aluminum Deposition and Dissolution in [EMIm]Cl-Based Ionic Liquids–Kinetics of Charge–Transfer and the Rate–Determining Step

Rene Böttcher,[*,z] Sebastian Mai, Adriana Ispas,[**] and Andreas Bund[**]

Electrochemistry and Electroplating Group, Department of Electrical Engineering and Information Technology, Technische Universität Ilmenau, 98693 Ilmenau, Germany

The kinetics of the dissolution and deposition of aluminum from a first generation ionic liquid consisting of $AlCl_3$/1-ethyl-3-methylimidazolium chloride (molar ratio 2:1) was studied. Electrochemical impedance spectroscopy shows that the double layer capacitance and the charge–transfer resistance depend on the state of the electrode surface. The impedance spectra are strongly influenced by mass transport. The rate–determining step of the aluminum deposition, as determined from the cathodic Tafel slope evaluated from current step experiments, was found to be either a chemical step, releasing the complexing agent chloride, while aluminum is in the divalent oxidation state ($AlCl_3^- \rightarrow AlCl_2 + Cl^-$) or an electron transfer from the divalent to the monovalent aluminum occurring twice for the overall reaction to occur once ($Al^{2+} + e^- \rightarrow Al^+$). The rate–determining step for aluminum dissolution was found to be the transfer of an electron from elemental aluminum to the monovalent oxidation state ($Al^0 \rightarrow Al^+ + e^-$). A linear slope in the low cathodic overpotential region of the Tafel plot suggests a change in the cathodic rate–determining step. The Tafel slope indicates a chemical step, releasing the complexing agent chloride, after the last electron transfer ($AlCl^- \rightarrow Al^0 + Cl^-$) to be the rate–determining step for overpotentials below 50 mV. Density functional theory calculations support the proposed reduction and oxidation mechanisms.

 [DOI: 10.1149/1945-7111/ab9c84]

Manuscript submitted April 28, 2020; revised manuscript received June 1, 2020. Published June 29, 2020.

Electrochemical deposition is an elegant method to prepare metallic coatings with tailored properties via the variation of the process parameters, such as current density, potential, temperature and electrolyte composition. The highly interesting element aluminum cannot be electrodeposited from protic solvents since its standard potential is much more negative than the proton reduction (−1.66 V vs NHE[1]). Aprotic electrolytes for the electrochemical deposition of aluminum[2–6] have been developed during the last decades. Some of those processes are based on volatile and highly flammable compounds which increases the costs for an industrial process. Ionic liquids (ILs) were shown to be suitable for the deposition of a number of reactive metals.[7]

One of the most intensely investigated ILs for the deposition of aluminum is the eutectic mixture of 1-ethyl-3-methylimidazolium chloride, [EMIm]Cl, and $AlCl_3$[7] with a molar excess of $AlCl_3$ (Eq. 1).[7–10] Due to its properties, such as high electrical conductivity, good thermal and electrochemical stability and a broad liquidus range, this IL is well suited for the deposition of functional coatings[8–10] as well as for applications in the field of energy storage and conversion.[11–18] It is generally accepted that the deposition of aluminum from ILs is only possible from Lewis acidic melts as they contain the easily reducible heptachloroaluminate anion, $Al_2Cl_7^-$. The tetrachloroaluminate anion, $AlCl_4^-$, prevalent in the neutral melts, has a more cathodic reduction potential than the imidazolium cation.[7]

$$4\ Al_2Cl_7^- + 3\ e^- \rightarrow Al + 7\ AlCl_4^- \qquad [1]$$

There are reports of multi—electron transfers for the deposition of niobium (3—electron step)[19] and zirconium (4—electron step),[20,21] but such systems seem to be rather rare. However, the simultaneous transfer of three electrons, as suggested in the net reaction (Eq. 1), is highly improbable because the activation energy for a multi—electron step is very high (> 400 kJ mol^{-1}).[22,23] Therefore, the consecutive transfer of three individual electrons with one being the rate—determining step (RDS) has to be assumed.[24,25] The RDS of the deposition and dissolution of aluminum has been identified for some electrolytes, including molten salts,[22,26] electrolytes based on tetrahydrofuran (THF)[27–29] and an IL based on N-(n-butyl)pyridinium chloride.[30] To the knowledge of the authors a systematic investigation of the charge—transfer mechanism of aluminum in ILs based on [EMIm]Cl has not been reported so far. Understanding charge transfer mechanism in this IL allows the development of improved electrolytes for both the deposition of functional aluminum coatings[7] and development of aluminum—based batteries with high energy and power density.[15,16,18]

Therefore, this paper focuses on the investigation of the kinetics of the deposition and dissolution of aluminum in Lewis acidic [EMIm]Cl/$AlCl_3$ ionic liquids. Cyclic voltammetry was used to acquire information on the reversibility of the aluminum deposition and dissolution. Electrochemical impedance spectroscopy and controlled current step experiments were employed to study the mechanisms as well as to determine the RDS of the deposition and dissolution of aluminum, respectively. Depending on the height of the amplitude of the controlled current or controlled potential step, the resulting transients provide valuable information about the diffusion coefficient of the electrochemically active species,[31,32] the nucleation behavior[33–38] and charge—transfer reaction.[39] Density functional theory (DFT) calculations were performed to assess if the suggested mechanisms are thermodynamically reasonable.

Experimental

Anhydrous $AlCl_3$ (granules, 99 %, abcr, Germany) and [EMIm]Cl (>98 %, Iolitec, Germany) were used to prepare the electrolytes. [EMIm]Cl was dried at 60 °C for two days to a moisture level below 100 ppm (determined by Karl—Fischer titration). Due to the exothermic reaction of $AlCl_3$ and [EMIm]Cl, the $AlCl_3$ was added in small amounts to the [EMIm]Cl until a molar ratio of 2.0:1 was reached. The temperature was kept below 80 °C to prevent thermal decomposition of the electrolyte. After stirring for 24 h the electrolyte had a slightly yellowish color. In the following this electrolyte is denoted in the text as [EMIm]Al_2Cl_7.

All electrochemical experiments were performed in a glove box filled with argon (VAC Atmospheres, USA; O_2 and H_2O levels < 0.5 ppm) using a model SP300 or VSP potentiostat/galvanostat (BioLogic, France). Tungsten rods (1.6 mm diameter) embedded in glass were used as working electrodes, WE, for cyclic voltammetry.

*Electrochemical Society Student Member.
**Electrochemical Society Member.
[z]E-mail: rene.boettcher@tu-ilmenau.de

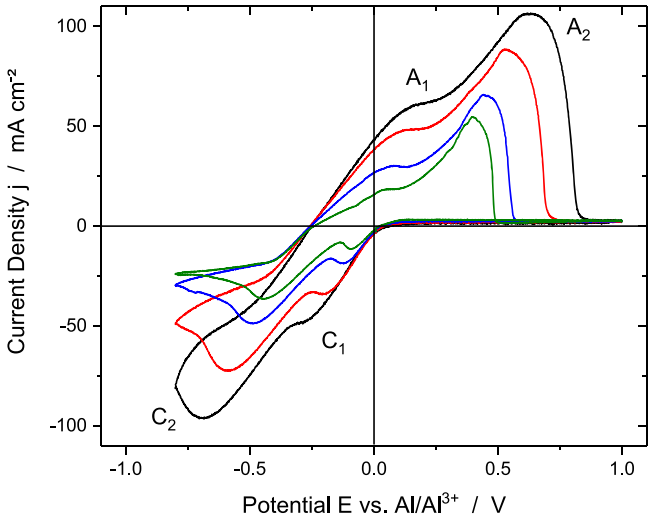

Figure 1. Cyclic voltammograms of a tungsten electrode in $[EMIm]Al_2Cl_7$ for sweep rates of 100 mV s^{-1} (black), 50 mV s^{-1} (red), 20 mV s^{-1} (blue) and 10 mV s^{-1} (green).

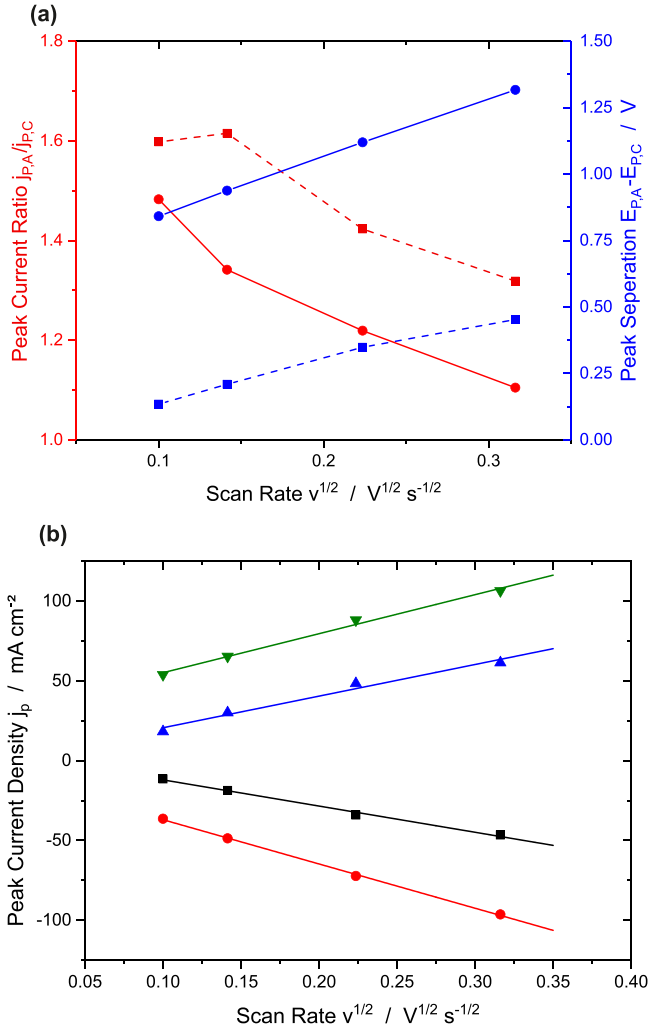

Figure 2. (a) Ratio of anodic and cathodic peak current density and peak separation of corresponding anodic and cathodic current waves A_1/C_1 (■ with dashed line) and A_2/C_2 (● with straight line) and (b) peak current density, j_P, vs scan rate, $v^{1/2}$, for current waves C_1 (■), C_2 (●), A_1 (▲) and A_2 (▼) and linear fit, derived from cyclic voltammograms in Fig. 1.

An aluminum wire (99.999 %, Alfa Aesar) with a diameter of 1 mm embedded in a glass tube and sealed with epoxy resin (Epoxy 2000 Plus, Cloeren Technology, Germany) was used as WE for electrochemical impedance spectroscopy (EIS) and the current step experiments. Before each experiment the aluminum WE was sanded with SiC emery paper (4000 grit). An aluminum plate (99.0 %, Good Fellow) of 2 mm thickness was used as a ring—shaped counter electrode (CE). An aluminum wire (99.999 %, Alfa Aesar) was used as the reference electrode (RE). In the following all potentials are given with respect to this reference.

Electrochemical impedance spectroscopy (EIS) measurements were performed using the aluminum WE in different conditions: Sanded with SiC emery paper (4000 grit) and coated with a thin aluminum layer of approximately 50 nm, respectively. The frequency was varied from 100 kHz down to 10 mHz (10 mV amplitude around OCP, 20 points per decade). Due to its size relative to the WE, the CE is assumed to be unpolarized and hence not to contribute to the impedance spectra. The electrode was kept at OCP (ca. 0 V) for 10 min before each measurement. In Fig. 3a, each marker represents the average value and standard deviation of the real part, Re(Z), and the imaginary part, Im(Z), of the impedance Z for one frequency, determined from five consecutive measurements.

DFT calculations for the formation enthalpy, ΔH_F, the solvation enthalpy, ΔH_S, and the reaction enthalpy, ΔH_R, were carried out using the M06-2X package of GAUSSIAN 20 Sep. Rev03 with the APCseg-2[40,41] and KTZVP-D base set[42] which was designed for organo—metallic thermodynamic calculations and has been shown to achieve accurate results. The works of Marchenich et al.[43] and Bernales et al.[44] prove the applicability of custom SMD models, solvation model based on density, for sufficiently accurate thermodynamic calculations of free solvent enthalpy values. Custom PCM-SMD model (polarizable continuum model with solvation model based on density) parameters, representing the $[EMIm]Cl/AlCl_3$ IL based on the work of Li et al.,[45] were chosen for the calculation of solvation enthalpy values. For the surface—attached species ΔH_s was approximated by only accounting for 50 % of the determined solvation enthalpy.

Results and Discussion

Cyclic voltammetry.—A typical cyclic voltammogram of aluminum deposition and stripping in $[EMIm]Al_2Cl_7$ on a tungsten electrode is shown in Fig. 1. The potential was swept starting from the OCP in cathodic direction down to −0.8 V and back to +1.0 V. The cathodic waves C_1 (−90 to −300 mV) and C_2 (−450 to −700 mV) can be attributed to the deposition of aluminum in nanocrystalline and microcrystalline form, respectively.[46] The anodic waves A_1 (60 to 200 mV) and A_2 (390 to 620 mV), are the corresponding stripping waves. The Coulombic efficiency for the deposition and dissolution of aluminum was around 98 %, calculated from 100 cycles at a sweep rate of 100 mV s^{-1}, which shows that aluminum can be deposited and dissolved without significant side reactions in this electrolyte. The separation of the peak potentials, $E_{P,A}$ and $E_{P,C}$, is larger than the theoretical value of 56.5 mV/n_e (n_e is the number of transferred electrons) for a fully reversible reaction at 298 K[24] (Fig. 2a) and increases with the sweep rate. This indicates kinetic limitations of the charge—transfer.[24,47] However, the ratio between anodic and cathodic peak current density, $j_{P,A}$ and $j_{P,C}$, plotted vs the square root of the scan rate, $v^{1/2}$, (Fig. 2b) shows a linear behavior in the range of 10 to 100 mV s^{-1} (error of the fitted slope typically lower than 5 %), indicating diffusion control.[23] Hence, the deposition and dissolution are influenced by the kinetics of the charge transfer and the diffusion of the electro-active species. Based on the considerations of Matsuda et al.[47] the deposition and dissolution process of aluminum in the present electrolyte should be categorized as quasi—reversible. Therefore, the equations of Randles and Sevcik[24,48,49] are not applicable in this case, since they are only

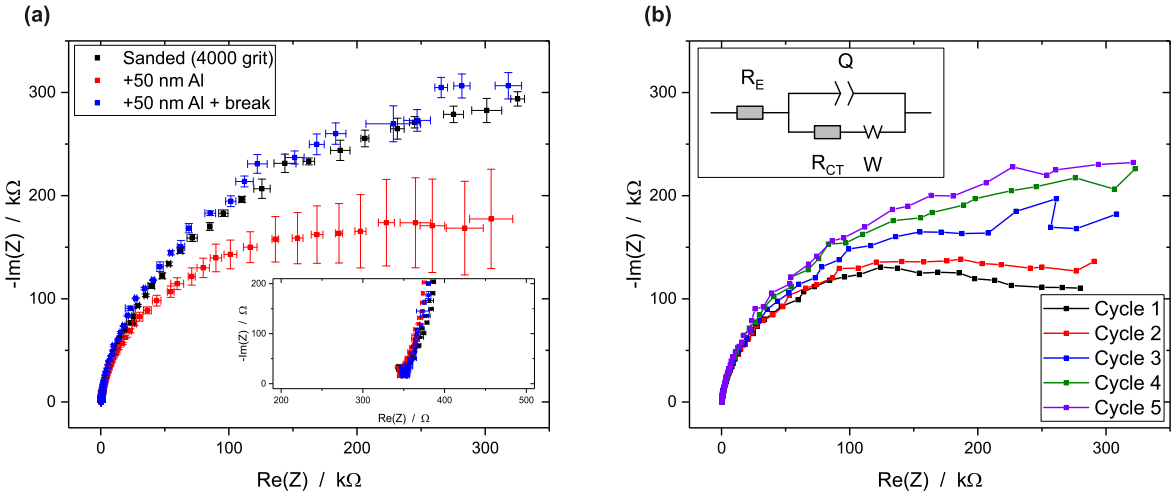

Figure 3. Electrochemical impedance spectra measured at an aluminum WE in a [EMIm]Al_2Cl_7: (a) Averaged spectra (five cycles) measured at a freshly sanded aluminum WE (black), a WE coated with 50 nm aluminum (red) and after resting for 12 h (blue). The inset shows the high frequency range. (b) Individual spectra (five consecutive cycles) measured at aluminum WE directly after coating with 50 nm aluminum. The inset shows the Randles equivalent circuit used to fit data.

valid for fully reversible and fully irreversible reactions. The peak separation is influenced by the Ohmic drop. Based on the distance between the WE and RE (ca. 1–2 mm), the surface area of the WE (ca. 2 mm^2) and the specific conductivity of the electrolyte (ca. 13.5 mS cm^{-1} at 27.5 °C), the Ohmic resistance between the WE and RE was estimated to be <1 Ω. Therefore, the associated shift of the peak potentials (Fig. 1) should be less than 2 mV and hence the peak separation due to Ohmic resistance (Fig. 2a) should be below 4 mV.

Electrochemical impedance spectroscopy (EIS).—The impedance spectra of an aluminum electrode at OCP (Fig. 3) can be described using the Randles equivalent circuit,[24,50] as displayed in the inset in Fig. 3b. The EIS spectra in the Nyquist representation have a depressed semicircle—like shape (Fig. 3a) with a rising portion in the low frequency region. This behavior can be described using a constant phase element (CPE), Q, in parallel to a resistor, representing the charge—transfer resistance, R_{CT}, and a Warburg element, W, modeling the influence of diffusion (Fig. 3b). The CPE can be described by the capacitance, Q, and a constant, α, (Eq. 2). If α is one the CPE behaves like an ideal capacitor, while it describes an Ohmic resistor if α is zero. The double layer capacitance, C_{eq}, and charge—transfer resistance, $R_{CT,eq}$, of an RC element, equivalent to the Randles equivalent circuit can be calculated from the values of the CPE and R_{CT}, which were previously determined by fitting of the EIS data (Eqs. 3 and 4).[51]

$$Z_{CPE} = Q^{-1} \cdot (i\omega)^{-\alpha} \quad [2]$$

$$C_{eq} = Q^{\frac{1}{\alpha}} \cdot R_{CT}^{\frac{1}{\alpha}-1} \quad [3]$$

$$R_{CT,eq} = \frac{R_{CT}}{2\left(\cos\left(\frac{\alpha\pi}{4}\right)\right)^2} \quad [4]$$

In passing we note that the double layer structure in ILs differs from aqueous solutions.[7,46,52,53] However, a detailed discussion about the structure of the electrode—IL interphase is beyond the focus of this work.

Independent of the state of the electrode surface (i. e. sanding or electrochemical coating with aluminum), the impedance spectra intercept the x—axis at (345 ± 25) Ω on average. This represents the Ohmic resistance of the electrolyte, R_E. Slight variations of the values are due to the relative positioning of the electrodes in the electrochemical cell.

Fit results of the EIS data using the Randles equivalent circuit are given in Table I. The value α of the CPE is typically very close to one (Table I). Deviations from the ideal capacitive behavior are probably caused by surface roughness effects (see Fig. 4 and discussion below). The capacitance (value of Q and C_{eq}, respectively) is smallest for the freshly sanded electrode and increases if aluminum is deposited on the electrode. The change in capacitance is caused by a change in the surface morphology (Fig. 4). Since the morphology does not or only slightly change during the resting period of 12 h at the OCP after coating, the capacity remains almost constant (Table I).

The charge—transfer resistance decreased after aluminum was deposited when compared to the sanded electrode surface. After the deposition the EIS spectrum changes over time (Fig. 3b). The capacitance remains constant while the charge—transfer resistance increases. The EIS spectra before the deposition of aluminum on the electrode and after 12 h of resting after deposition, are very similar (Fig. 3a). The change in charge transfer resistance indicates a time dependent interaction of the electrode with the IL. The chloroaluminate species or chloride anions (Eq. 13) might form an adsorbed layer or react with the freshly deposited aluminum. This layer might cause the described increase of the charge—transfer resistance. However, it is not clear from the presented results if the interaction of the IL with the deposit is caused by the $[EMIm]^+$ or the chloroaluminate species. On the other hand, the grown crystals might cause a larger surface area which results in the decrease of the apparent charge—transfer resistance. This micro roughness might be reduced by corrosion processes during the resting period, resulting in an increase of the charge—transfer resistance.

Overpotential measurements.— *Theoretical considerations.*—If a constant current is applied to an electrode, its overpotential, η, is the sum various contributions (Fig. 5 and Eq. 5).[24]

$$\eta = \eta_\Omega + \eta_{CT} + \eta_C + \eta_N + \eta_S \quad [5]$$

In Eq. 5, η_Ω is the Ohmic drop, η_{CT} is the charge—transfer overpotential, η_C is the concentration overpotential, η_N is the nucleation overpotential and η_S is the overpotential due to depletion of the electrolyte as a special case of the concentration overpotential.

The Ohmic resistance of the electrolyte, R_Ω, causes an instantaneous increase (η_Ω) at the moment the current density, j, is applied to

Table I. Data from fitting of the electrochemical impedance spectra displayed in Fig. 3a using the Randles equivalent circuit (inset of Fig. 3b).

Condition	RE/Ω	$Q/\mu Fs^{(\alpha-1)}$	α	$R_{CT}/k\Omega$	$s/\Omega s^{-1/2}$
Sanded	327 ± 4	1.37 ± 0.02	0.94	480 ± 20	114 ± 4
Coated	327 ± 4	2.03 ± 0.04	0.94	347 ± 41	27 ± 22
Coated + resting 12 h	326 ± 6	2.01 ± 0.02	0.94	572 ± 9	81 ± 2

Condition	$C_{eq}/\mu F$	$R_{CT,eq}/k\Omega$	$\tau_{DL}/\mu s$
Sanded	1.33 ± 0.01	437 ± 31	762 ± 13
Coated	1.99 ± 0.21	320 ± 19	651 ± 77
Coated + resting 12 h	2.01 ± 0.01	526 ± 5	655 ± 15

the electrode with the surface area, A, according to Ohm's law (Eq. 6).

$$\eta_{\Omega} = j \cdot A \cdot R_{\Omega} \quad [6]$$

The Ohmic resistance of the experimental setup was measured via electrochemical impedance spectroscopy (see section Electrochemical Impedance Spectroscopy) before each step experiment and was (345 ± 25) Ω on average. The overpotential increases by the value of $\eta_{CT}(t)$ within the time constant, τ_{DL}, due to double layer charging (Eqs. 7 and 8).[39]

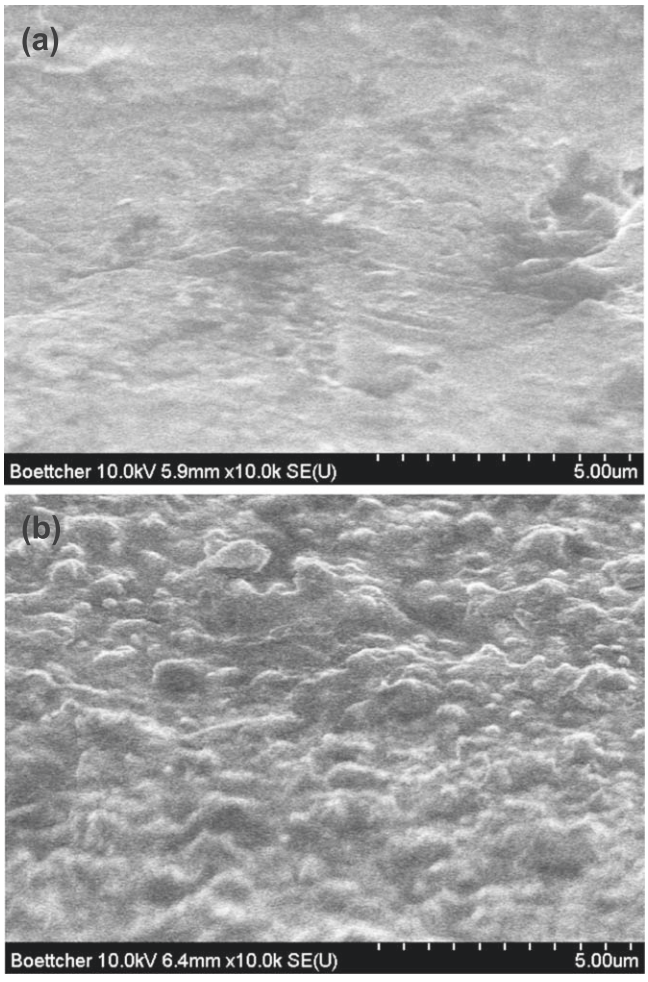

Figure 4. SEM micrograph of the surface of the aluminum electrode: (a) Sanded (4000 grit) and (b) after Al plating at −300 mV from $[EMIm]Al_2Cl_7$ for a passed electrical charge of 2 mC (corresponds to layer thickness of about 50 nm).

$$\eta_{CT}(t) = j \cdot A \cdot R_{CT,eq} \cdot \left(1 - \exp\left(-\frac{t}{\tau_{DL}}\right)\right) \quad [7]$$

$$\tau_{DL} = R_E \cdot C_{eq} \quad [8]$$

The time constant of the electrochemical double layer, τ_{DL}, was calculated from the double layer capacitance and the electrolyte resistance evaluated via impedance spectroscopy (see section Electrochemical Impedance Spectroscopy) and its value was below 800 μs (Table I). In a more refined approach one would have to consider that the value for the charge—transfer resistance decreases with increasing overpotential.[39] However, for the following discussion this estimation seems to be sufficient.

A concentration gradient evolves due to the electrochemical reaction in front of the electrode causing a time dependent concentration overpotential, $\eta_C(t)$ (Eq. 9).[54,55] The time τ_C which is needed to cause a decrease of the surface concentration by 10 % can be calculated by Eq. 11.[39]

$$\eta_C(t) = \frac{RT}{zF} \cdot ln\left(\frac{c(t)}{c^*}\right) \quad [9]$$

$$c(t) = c^* - \frac{2j}{zF} \cdot \left(\frac{t}{\pi D}\right)^{1/2} \quad [10]$$

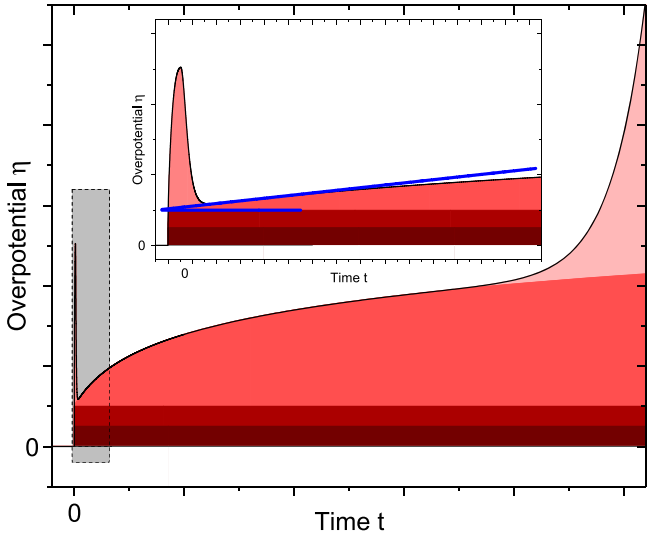

Figure 5. Schematic potential—time transient for a constant—current step based on Eq. 5. The inset shows the time range of the transient in the grey box. The transient consists of contributions from (dark red to light red) Ohmic resistance (Eq. 6), charge—transfer (Eqs. 7 and 8), concentration overpotential (Eqs. 9 and 11), nucleation and depletion (Eq. 12). Quantitative axis labeling was omitted due to the schematic character of the displayed transient.

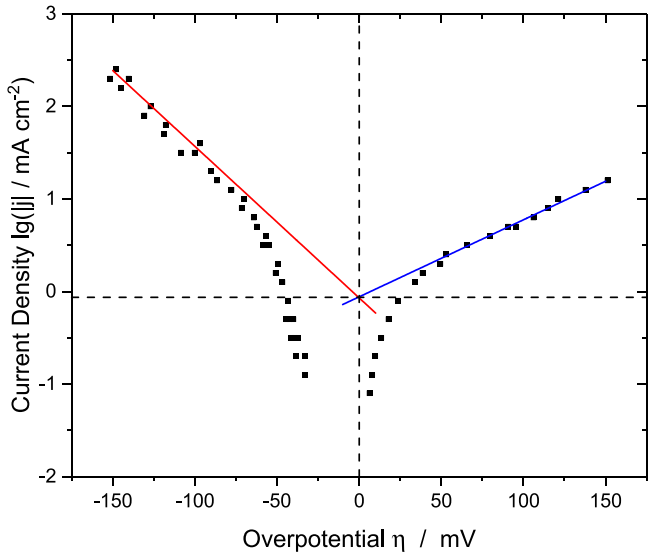

Figure 6. Tafel plot of overpotential data (dots) and Tafel fit for $|\eta| > 50$ mV (red and blue straight lines).

$$\tau_C = \frac{(0.1 \cdot zFc^*)^2 D\pi}{4j^2} \quad [11]$$

In Eqs. 9 to 11, R is the ideal gas constant, T is the temperature, z is the number of transferred electrons, F is the Faraday constant, $c(t)$ is the time dependent concentration at the electrode surface, c^* is the bulk concentration of the heptachloroaluminate anions in the electrolyte, (3.41 ± 0.01) mol L^{-1}, j is the current density and D is the diffusion coefficient of the heptachloroaluminate anions, (7.11 ± 0.31) × 10^{-11} m^2 s^{-1} (determined from potential and current step experiments according to Sand[31] and Cottrell,[32] data not shown). From these values τ_C was estimated to be longer than 0.3 s in this system.

Furthermore, if the applied current density is high, the mass transport towards the electrode surface is too slow to maintain the current and the concentration at the electrode surface decreases to zero after the transition time τ_S (Eq. 12).[31]

$$\tau_S = \frac{(zFc^*)^2 D\pi}{4j^2} \quad [12]$$

As a consequence of this depletion the overpotential increases (η_S) to a value that is high enough to drive an electrochemical process that is able to maintain the applied current density. For [EMIm]Al_2Cl_7 this is the electrochemical decomposition of [EMIm]$^+$. Equation 12 is a special case of Eq. 10 and leads to the Sand equation.[31] τ_S is 100 times longer than τ_C.

There is a further contribution to the total overpotential which arises from the nucleation of the deposited material on the electrode surface (η_N). There are several models describing transients influenced by nucleation based on constant potential steps[33–35,56] but only few based on constant current steps.[57–60] However, analytical expressions of the nucleation overpotential arising from a current step are not trivial to derive[57] and depend on various parameters, which are difficult to assess.[57,60] The nucleation peak displayed in Fig. 5 is a schematic representation of nucleation peaks observed in the experiments and is in agreement with the work of Milchev et al.[57] The nucleation peak in the potential-time transients has a typical duration of 0.1 to 0.5 s for the investigated system. A detailed discussion of galvanostatic nucleation transients is beyond the scope of this work and we take a phenomenological approach to consider the contribution η_N to the overall overvoltage.

Since nucleation peak and double layer charging overlap the potential response caused by the charge—transfer during the first several hundreds of μs, a straight forward evaluation of our data following the approach of Lorenz[39] would be strongly prone to systematic errors. Therefore, the overpotential due to charge—transfer was evaluated by a tangent of the rising part of the potential—time transient right after the nucleation peak ends and the double layer is fully charged (inset of Fig. 5 upper blue line). The potential value of this tangent at t = 0 gives an approximation for the sum of the overpotential caused by the charge—transfer and the Ohmic resistance (inset of Fig. 5 lower blue line). The charge—transfer overpotential can then be estimated by subtracting the Ohmic drop (Eq. 6). The latter was measured via electrochemical impedance spectroscopy prior to every current step experiment. With thus estimated values of η_{CT} the kinetics of the charge transfer will now be further discussed.

The overall reduction of aluminum as given in Eq. 1 can be divided into the electrochemical reaction involving the transfer of three of electrons while releasing one mole of $AlCl_4^-$ and three moles Cl^- (Eq. 13) and the chemical reaction of the released Cl^- with three moles $Al_2Cl_7^-$ forming six moles $AlCl_4^-$ (Eq. 14).[61] Hence the reduction mechanism consists of electrochemical and chemical steps. The net reaction (Eq. 15) is then in agreement with Eq. 1.

$$Al_2Cl_7^- + 3\,e^- \rightarrow Al + AlCl_4^- + 3\,Cl^- \quad [13]$$

$$3\,Al_2Cl_7^- + 3\,Cl^- \rightarrow 6\,AlCl_4^- \quad [14]$$

$$4\,Al_2Cl_7^- + 3\,e^- \rightarrow Al + 7\,AlCl_4^- \quad [15]$$

Determination of the rate—determining step (RDS).—The logarithm of the current density vs the charge—transfer overpotential is plotted in Fig. 6. In order to find the most probable rate—determining step (RDS) of the anodic and cathodic reaction, the Tafel slopes were compared with the theoretical values based on the assumption that the net reaction is a sequence of three individual one—electron transfer processes.[24] The theoretical anodic and cathodic reciprocal Tafel slopes b_a and b_c are calculated according to Eqs. 16 and 17.[25,29,62]

$$b_a = \frac{RT}{F\left(\frac{\gamma_f}{\nu} + (1 - \beta_a)r\right)} \quad [16]$$

$$b_c = \frac{RT}{F\left(\frac{\gamma_p}{\nu} + \beta_c r\right)} \quad [17]$$

with the number of transferred electrons before, during and after the RDS, γ_p, r and γ_f, the stoichiometric number ν describing how often the RDS needs to occur for the overall reaction to occur once and the anodic and cathodic symmetry factor β_a and β_c (here assumed to be 0.5).

For absolute overpotentials beyond 50 mV the experimental data give reciprocal Tafel slopes of (120 ± 2) mV dec^{-1} and (61 ± 4) mV dec^{-1} for the anodic and cathodic reaction, respectively (Fig. 6). The simplest and hence most probable RDS for the anodic reaction is the oxidation of metallic aluminum to monovalent aluminum ($Al^0 \rightarrow Al^+ + e^-$, theoretical value 120 mV dec^{-1}).

The overall calculated anodic charge—transfer coefficient, α_a, is 0.17 ± 0.01 and the resulting symmetry factor, β_a, is then 0.62 ± 0.01, based on the theoretical considerations for the most probable RDS. An exchange current density, j_0, of (0.88 ± 0.02) mA cm^{-2} was calculated from the anodic Tafel slope. The dissolution mechanism of aluminum in a 2.0:1 electrolyte can be proposed as

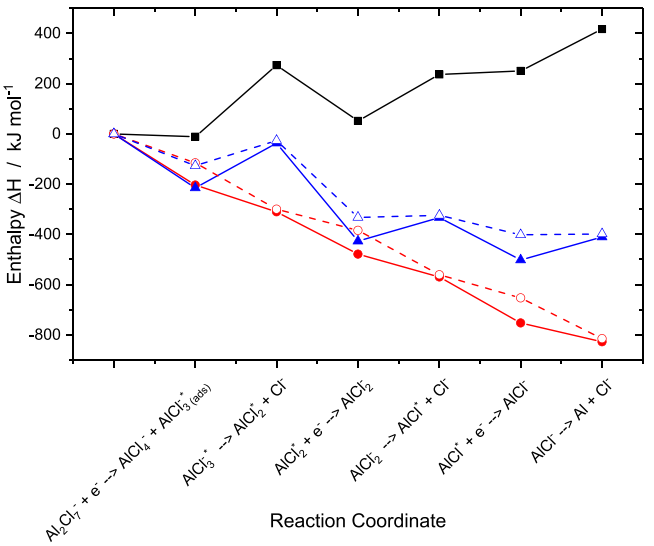

Figure 7. Change in enthalpy for the reduction of aluminum according to the reduction sequence in Scheme 2 (left) calculated using KTZVP-D base set: Formation enthalpy (■), solvation enthalpy (●), reaction enthalpy (▲), corrected solvation enthalpy (○) and corrected reaction enthalpy (△). The difference in the results of the calculations using APCseg-2 base set and KTZVP-D base set lies within the markers.

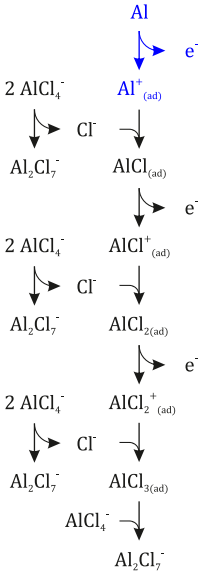

Scheme 1. Flow chart for aluminum dissolution. The suggested RDS is colored in blue.

shown in Scheme 1, considering three separate one—electron transfers and chemical steps releasing chloride ions which is in agreement with Eq. 15.

There are different possible RDS reactions for the cathodic reaction based on the experimental Tafel slope. On one hand the RDS might be a chemical step while aluminum is in the oxidation state two (theoretical value 60 mV dec^{-1}), releasing the complexing agent chlorine, according to Eq. 18.

$$AlCl_3^-{}_{(ad)} \rightarrow AlCl_{2(ad)} + Cl^- \quad [18]$$

Considering a sequence of single electron transfers and chemical steps releasing chlorine ions, the deposition mechanism in Scheme 2 (left) can be proposed.

On the other hand, the RDS might be the reduction of divalent to monovalent aluminum with $\nu = 2$ (theoretical value 60 mV dec^{-1}),

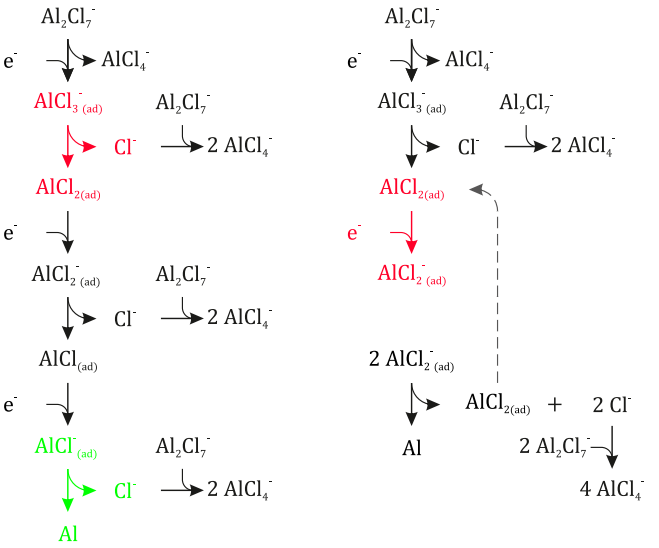

Scheme 2. Flow chart for aluminum deposition (left: chemical RDS; right: electrochemical RDS). The suggested low overpotential RDS ($\eta < 50$ mV) is colored in green, the suggested high overpotential RDS ($\eta > 50$ mV) is colored in red.

according to Eq. 19. The subsequent reduction might then occur according to Eq. 20.

$$Al^{2+} + e^- \rightarrow Al^+ \quad [19]$$

$$2\ Al^+ \rightarrow Al + Al^{2+} \quad [20]$$

The deposition mechanism can be proposed as shown in Scheme 2 (right). The symmetry factor, β_c, was calculated to be 0.25 ± 0.05.

The overall cathodic charge—transfer coefficient, α_c, and the exchange current density, j_0, were found to be 0.33 ± 0.03 and (0.85 ± 0.12) mA cm^{-2}, respectively. The anodic and cathodic exchange current density evaluated from the respective Tafel slopes are in good agreement with each other and give an average value of (0.87 ± 0.07) mA cm^{-2}.

While the logarithm of the current density decreases with decreasing overpotential in a non—linear fashion in the anodic range, an additional linear region with a reciprocal Tafel slope of (17 ± 2) mV dec^{-1} can be found in the cathodic range between 30 and 50 mV (Fig. 6, linear fit not shown). This suggests a change of the RDS between low and high overpotentials. Since the Tafel approximation loses accuracy for absolute overpotentials below 50 mV, it is not trivial to estimate the Tafel slope. The deviation from the Tafel approximation increases with decreasing overpotential. Based on the kinetic values for charge transfer coefficients and exchange current density, as discussed above, the deviation is below 20 % for overpotentials beyond 30 mV. The Tafel slope of (17 ± 2) mV dec^{-1} is close to the theoretical value of a RDS consisting of a chemical step after aluminum was fully discharged (theoretical value 20 mV dec^{-1}), according to Eq. 21.

$$AlCl^-{}_{(ad)} \rightarrow Al + Cl^- \quad [21]$$

Ali et al.[30] reported a similar behavior of the deposition of aluminum from a Lewis acidic mixture of $AlCl_3$ and N-(n-butyl)pyridinium chloride in a comparable low cathodic overpotential range. This step is in agreement with the deposition mechanism proposed in Scheme 2 (left).

The change in the Tafel slope occurs at approximately −60 mV (Fig. 6). The crystallization mode of aluminum changes in the range of −40 and −80 mV for steady state conditions (extrapolated cathodic peak potentials from Fig. 1), suggesting a relation between

the RDS, the crystallization in a nanocrystalline and microcrystalline structure.

All proposed dissolution and deposition mechanism for aluminum from a 2.0:1 electrolyte (Schemes 1 and 2) are consistent with the overall reaction according to Eq. 1.

Thermodynamic considerations using density functional theory (DFT).—For the theoretical anodic RDS describing a chemical reaction prior to the oxidation from metallic to monovalent, γ_f and r equal zero (Eq. 16). For the theoretical cathodic RDS describing a chemical reaction prior to the reduction from trivalent to divalent aluminum, γ_p and r equal zero (Eq. 17). Therefore, mathematically there are no solutions for these cases, according to Eqs. 16 and 17 (devision by zero). On this basis a reaction sequence for the oxidation of metallic aluminum to form $Al_2Cl_7^-$ as well as for the reduction of $Al_2Cl_7^-$ to metallic aluminum is suggested (Schemes 1 and 2).

The proposed anodic reaction sequence (Scheme 1) consists of the oxidation of the metallic aluminum to an adsorbed monovalent aluminum ($Al^+_{(ad)}$). By forming the heptachloroaluminate from two tetrachloroaluminate anions a chloride ion is available for the speciation of $AlCl_{(ad)}$. The overall enthalpy of the transfer of a chloride ion from tetrachloroaluminate anions to the adsorbed aluminum ion is negative and therefore thermodynamically reasonable. The $AlCl_{(ad)}$ is then further oxidized to $AlCl^+_{(ad)}$, representing the divalent state of aluminum. Binding another chloride ($AlCl_{2(ad)}$) represents the RDS in the anodic reaction sequence (Scheme 1). After the third electron transfer forming trivalent aluminum ($AlCl_2^+{}_{(ad)}$) and binding a third chloride the oxidation sequence is complete and has consumed seven moles of $AlCl_4^-$ to produce four moles of Al_2 Cl_7^- while transferring three electrons (Eq. 15).

The oxidation of aluminum (neglecting the bound chloride) and the subsequent chemical reactions can then be generally expressed as

$$Al^n \rightarrow Al^{n+1} + e^- \quad [22]$$

$$AlCl_n^+ + Cl^- \rightarrow AlCl_{n+1} \quad [23]$$

with n = 0…2.

Since the proposed cathodic reaction presented in Scheme 2 (left) includes the RDS for high cathodic overpotentials as well as for low overpotentials, the following discussion focuses on this sequence. This sequence is initiated with the reduction of trivalent aluminum from $Al_2Cl_7^-$ to adsorbed $AlCl_3^-{}_{(ad)}$ releasing $AlCl_4^-$. The adsorbed species decomposes to $AlCl_{2(ad)}$ releasing chloride which reacts with $Al_2Cl_7^-$ to two $AlCl_4^-$. The following reduction step to monovalent aluminum $AlCl_2^-{}_{(ad)}$ represents the RDS of the cathodic sequence (Scheme 2, left). After decomposing to $AlCl_{(ad)}$, releasing another chloride, the reduction to $AlCl^-_{(ad)}$ occurs, followed by a last chemical step releasing chloride and forming metallic aluminum at the electrode surface.

The reduction of aluminum (neglecting bound chloride) and the subsequent chemical reactions can be generally expressed as

$$Al^n + e^- \rightarrow Al^{n-1} \quad [24]$$

$$AlCl_n^- + Cl^- \rightarrow AlCl_{n-1} + Cl^- \quad [25]$$

with n = 3…1.

DFT calculations were carried out to clarify whether the reduction and oxidation sequences presented above are thermodynamically reasonable. The contribution of the adsorption of the reactants was assumed to be approximately constant and therefore neglected. Figure 7 presents the change in enthalpy for the formation of the reactants, ΔH_F, solvation, ΔH_s, and their sum, the reaction enthalpy, ΔH_R (Eq. 26).

$$\Delta H_R = \Delta H_F + \Delta H_S \quad [26]$$

While the formation enthalpy over the reaction coordinate increases, the solvation enthalpy, representing the interaction of the IL with the formed products, decreases. The contribution of the solvation enthalpy is bigger than that of the formation enthalpy, presumably because of the high space charge density of the reduced intermediates. The reaction enthalpy is negative, suggesting that the overall reaction is spontaneous from a thermodynamic perspective. Since this is not the case in the experiment one must assume that the kinetic barrier between any of the discussed reaction steps in either direction must be high enough to keep a reaction from occurring at even elevated temperatures used in the experiment. The enthalpy data result from the respective reaction without taking into account the influence of the electrode surface which the reactants are adsorbed on. Modeling metal—metal interactions using DFT to simulate the electrode surface is not trivial and requires a high computational effort. Therefore, a simple geometrical approach was chosen. The adsorbed reactants interact with the electrode surface at one side. This reduces the available surface area to interact with the electrolyte. Therefore, the resulting solvation enthalpy of these adsorbed reactants, $\Delta H_{S,ad}$, is reduced by a factor of two, while the solvation enthalpy of the solvated reactants, $\Delta H_{S,sol}$, remains as before (Eq. 27).

$$\Delta H_{R,corr} = \Delta H_F + 0.5\,\Delta H_{S,ad} + \Delta H_{S,sol} \quad [27]$$

The corrected values are displayed in Fig. 7 and show that the previously described tendency did not change significantly as the main part of ΔH_S is due to the solvation of Cl^- species.

Conclusions

Cyclic voltammetry measurements show the quasi—reversible character of the aluminum deposition and dissolution in $[EMIm]Al_2Cl_7$ with a Coulombic efficiency close to 100%.

Electrochemical impedance spectroscopy suggests that the fresh electrodeposited aluminum film interacts with the electrolyte. This might be either the formation of a passive film on the surface (e.g. adsorbing chloroaluminate complexes) or corrosion of the deposit in the electrolyte leading to a reduced micro roughness. Superposition of both processes might be possible, too.

The potential—time transients were interpreted and discussed considering different contributions to the overall overpotential. Based on these considerations a method was described to estimate values for the sum of Ohmic drop and charge transfer overpotential. The Ohmic drop was calculated based on EIS results regarding the Ohmic resistance of the electrolyte. The transfer coefficients and the exchange current density for aluminum deposition and dissolution were evaluated from the plot of current density vs charge transfer overpotential. From the values of the reciprocal Tafel slopes the RDS for aluminum deposition and dissolution were suggested. The RDS for the oxidation of aluminum is probably the electron transfer from elemental aluminum to the monovalent oxidation state. A linear range in the low cathodic overpotential region (<50 mV) and another one in the high cathodic overpotential region (>50 mV) suggest a change in the RDS. For the low overpotential range, the RDS is probably a chemical step after the last electron transfer. For the high overpotential range, the RDS is either a chemical step while aluminum is in the divalent oxidation state or an electron step from divalent to monovalent aluminum, which need to occur twice for the overall reaction to occur once. DFT calculations show that the proposed sequences for the deposition and dissolution of aluminum, given in Schemes 1 and 2, are thermodynamically reasonable, since solvation enthalpy, primarily delivered by chloride ions, makes aluminum deposition in $[EMIm]Al_2Cl_7$ a thermodynamically favorable process.

Acknowledgments

The authors gratefully acknowledge the financial support of the German Federal Ministry of Economic Affairs and Energy (Bundesministerium für Wirtschaft und Energie), within the project NiCO (ref. no. 20W1523H). Thanks also go to Mohammadshahabaldin Najafi for the assistance in the electrochemical measurements.

ORCID

Rene Böttcher https://orcid.org/0000-0001-9016-4129
Adriana Ispas https://orcid.org/0000-0001-8203-7752
Andreas Bund https://orcid.org/0000-0001-9837-2408

References

1. D. R. Lide (ed.), *CRC Handbook of Chemistry and Physics: A Ready-Reference Book of Chemical and Physical Data* (CRC press, Boca Raton, Florida) (1996).
2. K. Ziegler and H. Lehmkuhl, *Z. Anorg. Allg. Chem.*, **283**, 414 (1956).
3. W. Kautek and S. Birkle, *Electrochim. Acta*, **34**, 1213 (1989).
4. H. Lehmkuhl, K. Mehler, and U. Landau, *Adv. Electrochem. Sci. Eng.*, **3**, 163 (1993).
5. N. Ishibashi and M. Yoshio, *Electrochim. Acta*, **17**, 1343 (1972).
6. M. Yoshio and N. Ishibashi, *J. Appl. Electrochem.*, **3**, 321 (1973).
7. F. Endres, A. Abbott, and D. MacFarlane, *Electrodeposition from Ionic Liquids* (Wiley-VCH, Weinheim) 2nd ed. (2017).
8. T. Jiang, M. C. Brym, G. Dubé, A. Lasia, and G. M. Brisard, *Surf. Coat. Tech.*, **201**, 1 (2006).
9. A. Bakkar and V. Neubert, *Electrochim. Acta*, **103**, 211 (2013).
10. H. M. A. Abood and N. L. Dawood, *Int. J. Res. Sci.*, **4**, 753 (2015).
11. N. Jayaprakash, S. K. Das, and L. A. Archer, *Chem. Comm.*, **47**, 12610 (2011).
12. M. Ueda, H. Matsunaga, and T. Ohtsuka, *Z. Phys. Chem.*, **227**, 1097 (2013).
13. J. V. Rani, V. Kanakaiah, T. Dadmal, M. S. Rao, and S. Bhavanarushi, *J. Electrochem. Soc.*, **160**, A1781 (2013).
14. S. Wang, Z. Yu, J. Tu, J. Wang, D. Tian, Y. Liu, and S. Jiao, *Adv. Energy Mater.*, **6**, 1600137 (2016).
15. T. Schoetz, C. P. de Leon, M. Ueda, and A. Bund, *J. Electrochem. Soc.*, **164**, A3499 (2017).
16. C. Ferrara, V. Dall'Asta, V. Berbenni, E. Quartarone, and P. Mustarelli, *J. Phys. Chem. C*, **121**, 26607 (2017).
17. T. Schoetz, M. Ueda, A. Bund, and C. Ponce de Leon, *J. Solid State Electrochem.*, **21**, 3237 (2017).
18. T. Schoetz, B. Craig, C. P. de Leon, A. Bund, M. Ueda, and C. T. J. Low, *Journal of Energy Storage*, **28**, 101176 (2020).
19. S. Senderoff and G. W. Mellors, *J. Electrochem. Soc.*, **113**, 66 (1966).
20. G. W. Mellors and S. Senderoff, *J. Electrochem. Soc.*, **113**, 60 (1966).
21. D. L. Manning and G. Mamantov, *J. Electroanal. Chem.*, **6**, 328 (1963).
22. B. S. Del Duca, *J. Electrochem. Soc.*, **118**, 405 (1971).
23. R. Guidelli, R. G. Compton, J. M. Feliu, E. Gileadi, J. Lipkowski, W. Schmickler, and S. Trasatti, *Pure Appl. Chem.*, **86**, 245 (2014).
24. A. J. Bard and L. R. Faulkner, *Electrochemical Methods: Fundamentals and Applications* (John Wiley and Sons, New York) 2nd ed. (2001).
25. J. O. 'M. Bockris, Z. Nagy, and A. Damjanovic, *J. Electrochem. Soc.*, **119**, 285 (1972).
26. A. Sterten and P. A. Solli, *J. Appl. Electrochem.*, **25**, 809 (1995).
27. J. Eckert and M. Galova, *Electrochim. Acta*, **26**, 1169 (1981).
28. M. W. M. Graef, *J. Electrochem. Soc.*, **132**, 1038 (1985).
29. W. A. Badawy, B. A. Sabrah, and N. H. Y. Hilal, *J. Appl. Electrochem.*, **17**, 357 (1987).
30. M. R. Ali, A. Nishikata, and T. Tsuru, *Indian J. Chem. Techn.*, **6**, 317 (1999).
31. H. J. S. Sand, *Lond. Edinb. Dubl. Phil. Mag.*, **1**, 45 (1901).
32. F. G. Cottrell, *Z. Phys. Chem.*, **42U**, 386 (1903).
33. B. Scharifker and G. Hills, *Electrochim. Acta*, **28**, 879 (1983).
34. B. R. Scharifker and J. Mostany, *J. Electroanal. Chem.*, **177**, 13 (1984).
35. L. Heerman and A. Tarallo, *J. Electroanal. Chem.*, **470**, 70 (1999).
36. M. Palomar-Pardavé, B. R. Scharifker, E. M. Arce, and M. Romero-Romo, *Electrochim. Acta*, **50**, 4736 (2005).
37. V. A. Isaev, O. V. Grishenkova, and Y. P. Zaykov, *J. Electroanal. Chem.*, **818**, 265 (2018).
38. V. A. Isaev, Y. P. Zaykov, O. V. Grishenkova, A. V. Kosov, and O. L. Semerikova, *J. Electrochem. Soc.*, **166**, D851 (2019).
39. W. Lorenz and B. Bunsenge, *Phys. Chem.*, **58**, 912 (1954).
40. F. Jensen, *J. Chem. Phys.*, **115**, 9113 (2001).
41. F. Jensen, *J. Chem. Phys.*, **117**, 9234 (2002).
42. A. Schäfer, C. Huber, and R. Ahlrichs, *J. Chem. Phys.*, **100**, 5829 (1994).
43. A. V. Marenich, C. J. Cramer, and D. G. Truhlar, *J. Phys. Chem. B*, **113**, 6378 (2009).
44. V. S. Bernales, A. V. Marenich, R. Contreras, C. J. Cramer, and D. G. Truhlar, *J. Phys. Chem. B*, **116**, 9122 (2012).
45. H. Li, Y. Chang, W. Zhu, W. Jiang, M. Zhang, J. Xia, S. Yin, and H. Li, *J. Phys. Chem. B*, **119**, 5995 (2015).
46. A. P. Abbott, F. Qiu, H. M. A. Abood, M. R. Ali, and K. S. Ryder, *Phys. Chem. Chem. Phys.*, **12**, 1862 (2010).
47. H. Matsuda and Y. Ayabe, *Ber. Bunsenge. Phys. Chem.*, **59**, 494 (1955).
48. P. Zanello, *Inorganic Electrochemistry: Theory, Practice and Application* (Royal Society of Chemistry, Cambridge) (2003).
49. W. Vielstich, *Handbook of fuel Cells: Fundamentals, Technology and Applications*, ed. W. Vielstich (Wiley Interscience, Hoboken, New Jersey) (2010).
50. J. E. B. Randles, *Faraday Discuss.*, **1**, 11 (1947).
51. J.-P. Diard, B. Le Gorrec, and C. Montella, *Handbook of Electrochemical Impedance Spectroscopy*, BioLogic (2013), https://bio-logic.net/wp-content/uploads/QCircuits.pdf.
52. M. Drüschler, *Elektrochemische Untersuchungen zur Struktur und Dynamik der Grenzfläche zwischen ionischen Flüssigkeiten und Au (111)*, Philipps-Universität Marburg (2013), Dissertation.
53. Y. Zheng, Y. Zheng, C. Peng, Z. Zhao, and D. Tian, *Int. J. Electrochem. Sci.*, **11**, 9585 (2016).
54. M. Noponen, T. Hottinen, T. Mennola, M. Mikkola, and P. Lund, *J. Appl. Electrochem.*, **32**, 1081 (2002).
55. S. K. Murthy, A. K. Sharma, C. Choo, and E. Birgersson, *J. Electrochem. Soc.*, **165**, A1746 (2018).
56. P. Altimari and F. Pagnanelli, *Electrochim. Acta*, **205**(Supplement C), 113 (2016).
57. A. Milchev and M. I. Montenegro, *J. Electroanal. Chem.*, **333**, 93 (1992).
58. W. F. Schottky and Z. Phys, *Chem. Neue Fol.*, **31**, 40 (1962).
59. N. A. Saltykova, O. L. Semerikova, and L. T. Kosikhin, *Russ. J. Electrochem.*, **37**, 1034 (2001).
60. D. Kashchiev, *Thin Solid Films*, **29**, 193 (1975).
61. S. Schaltin, M. Ganapathi, K. Binnemans, and J. Fransaer, *J. Electrochem. Soc.*, **158**, D634 (2011).
62. J. O. 'M. Bockris and A. K. N. Reddy, *Modern electrochemistry: An introduction to an interdisciplinary area* (Plenum Press, New York) 3rd ed. (1977).